RESEARCH ARTICLE | AUGUST 26 2025

Particle levitation velocimetry for boundary layer measurements in high Reynolds number liquid helium turbulence

Yinghe Qi (漆映荷) ; Wei Guo (郭伟)

Physics of Fluids 37, 085248 (2025)
https://doi.org/10.1063/5.0287550

Physics of Fluids ARTICLE pubs.aip.org/aip/pof

Particle levitation velocimetry for boundary layer measurements in high Reynolds number liquid helium turbulence

Cite as: Phys. Fluids **37**, 085248 (2025); doi: 10.1063/5.0287550
Submitted: 25 June 2025 · Accepted: 2 August 2025 ·
Published Online: 26 August 2025

View Online Export Citation CrossMark

Yinghe Qi (漆映荷) and Wei Guo (郭伟)[a)]

AFFILIATIONS

National High Magnetic Field Laboratory, 1800 East Paul Dirac Drive, Tallahassee, Florida 32310, USA
and Mechanical Engineering Department, FAMU-FSU College of Engineering, Tallahassee, Florida 32310, USA

[a)]Author to whom correspondence should be addressed: wguo@magnet.fsu.edu

ABSTRACT

Accurate measurement of near-wall velocity fields in high Reynolds number (Re) turbulent boundary layer flows is critically important, yet presents significant experimental challenges. Generating such flows requires complex, power-intensive, large-scale facilities, and the use of local probes, such as hot wires and pressure sensors, often introduces disturbances due to the necessary support structures, thereby compromising measurement accuracy. In this paper, we present a solution that leverages the vanishingly small viscosity of liquid helium to produce high Re flows, combined with a proposed particle levitation velocimetry (PLV) system for precise flow-field measurements. This PLV system uses magnetically levitated superconducting micro-particles to measure the near-wall velocity field in liquid helium. Through comprehensive theoretical analysis, we demonstrate that the PLV system enables quantitative measurements of the velocity boundary layer over a wall unit range of $44 \leq y^+ \leq 4400$, with spatial resolution down to about 10 μm, depending on particle size. This development opens new avenues for exploring turbulence structures and correlations within the thin boundary layer that would be otherwise difficult to achieve.

I. INTRODUCTION

Turbulent boundary layer flows are fundamental to numerous engineering applications. For instance, dissipation in these flows controls aerodynamic forces and heating in hypersonic vehicles and accounts for over 50% of surface drag in aircraft, as well as nearly 95% of energy loss in long-distance pipeline transport.[1,2] Many of these applications involve flows at very high Reynolds numbers (Re), where the turbulent boundary layer is characterized by near-wall small-scale structures, such as streaks and vortices, as well as larger, energetic eddies in the outer region.[3,4] The interaction between these scales at high Re intensifies turbulence and increases the complexity of flow dynamics. To better understand these interactions, it is crucial to precisely quantify turbulence characteristics within the boundary layer, including the scaling behaviors of mean velocity and turbulence intensity. This knowledge is vital for developing more accurate and predictive turbulence models, which are essential for optimizing designs and enhancing performance in practical engineering applications.

The mean velocity profile $\bar{U}_x(y)$ in the streamwise direction near a solid wall in fully developed turbulent flows has been studied extensively and is known to consist of three distinct regions along the coordinate y perpendicular to the wall.[3–5] The inner region, dominated by viscous effects, typically extends from the wall to $y^+ = y/y^* = 50$, where $y^* = \nu/u_\tau$ denotes the viscous length scale.[6] In this expression, ν is the kinematic viscosity, and $u_\tau = (\tau_w/\rho_f)^{1/2}$ is the viscous velocity, with τ_w being the wall shear stress and ρ_f the fluid density. At sufficiently large y, for example, beyond $y/R \approx 0.12$ in pipe flows with a pipe radius R, the wake region emerges, where $\bar{U}_x(y)$ depends on overall flow conditions. Between these two regions lies the overlap region, where $\bar{U}_x(y)$ follows a universal logarithmic profile, commonly referred to as the "law of the wall" or "log law," expressed as $U^+ = \frac{1}{\kappa}\ln y^+ + B$.[3–5] Here, $U^+ = \bar{U}_x/u_\tau$, and κ and B are the von Kármán constant and the additive constant, respectively. Despite extensive experimental[7–12] and numerical[13–15] investigations, some key issues remain unsolved, such as the extent and Re dependence of the log law and the precise values of these constants.[16,17] The Princeton Superpipe experiments suggest that the log law appears in the range $600 \leqslant y^+ \leqslant 0.12R/y^*$ when the pipe Reynolds number exceeds about 2.3×10^5.[3,7,18,19] These experiments reported a von Kármán constant $\kappa = 0.42$, which differs from the typical values of 0.37–0.39 observed in high-Re boundary layer and channel flows,[10,12,20–22] raising questions

about the universality of κ across different flow types. However, more recent high-Re pipe flow data from Furuichi *et al.*, using the "Hi-Reff" facility in Japan, suggest a κ value of 0.385, indicating a potential degree of universality for κ.[8,23] Given the pivotal role of κ in modeling and numerical simulations of wall-bounded flows, further independent high-Re flow measurements are necessary.

In high-Re turbulence experiments, velocity field measurements have predominantly relied on hot-wire anemometers and pressure sensors.[24–26] These sensors normally have relatively large sizes, limiting their spatial resolution and effectiveness in capturing the fine details of boundary layer flows. For instance, conventional hot-wire sensors are difficult to reduce below 0.25 mm in length. In response, efforts have been made to miniaturize these sensors. As an example, Smits' team developed hot-wire sensors with an active length as small as 30 μm.[7,27] Similarly, advances have also been made in pressure sensor technology.[28] However, despite these miniaturization efforts, both types of sensors still face one challenging issue: they require support structures attached to the wall, which inevitably introduce flow disturbances. These disturbances could compromise the collection of clean data in high-Re turbulent flows, particularly in thin boundary layers, where minimizing interference is crucial for accurate measurements. In addition to hot-wire anemometry and pressure sensors, non-intrusive measurement techniques based on direct flow visualization have been widely applied to measure velocity fields in various types of flows. Particle image velocimetry (PIV) and particle tracking velocimetry (PTV) are two commonly used flow visualization methods.[29–38] Usually, both methods face limitations in spatial resolution when applied to velocity field measurements in high-Re turbulent boundary layers, restricting their ability to resolve thin boundary layer structures.[39,40] Researchers from German Aerospace Center (DLR) and affiliated institutions have made progress in addressing resolution challenges in high-Reynolds-number boundary layer measurements. Their facility covers a wide Re range of $6 \times 10^4 \leq Re \leq 10^6$,[41,42] achieving wall-normal resolution of 6 pixels for $5400 \leq Re_\tau \leq 40000$ through a tailored implementation of PIV enabled two-component–two-dimensional (2C–2D) velocity measurements.[43] A combined PIV–PTV approach with wall correction was employed to balance field-of-view and resolution, with PIV providing 350 μm resolution over large areas, and PTV resolving near-wall structures at 3.2 μm.[44] Although PTV enables high resolution close to the wall, it is limited to discrete, time-varying particle locations, making it difficult to compute spatial averages, gradients, and correlations. These studies also highlight the inherent tradeoffs between spatial coverage and resolution—an issue that continues to motivate alternative measurement strategies. Another non-intrusive technique is molecular tagging velocimetry (MTV), which has been applied in various flow conditions, including studies of wall shear stress and velocity profiles.[45–51] However, typical MTV setups can only capture the velocity component perpendicular to the tracer lines, and their spatial resolution is constrained by the displacement of the tracer lines, typically on the order of 10^2 μm.[52] This limitation reduces its effectiveness for capturing fine-scale boundary layer structures in high-Re turbulence.

To overcome these limitations, we propose an approach that combines liquid helium (LHe) as the working fluid with a novel measurement technique called particle levitation velocimetry (PLV), which utilizes magnetically levitated superconducting micro-particles as probes. LHe's exceptionally low kinematic viscosity, i.e., nearly three orders of magnitude lower than that of ambient air,[53] allows for the generation of very high-Re flows in compact facilities,[54–56] which is difficult to achieve with conventional fluids. Moreover, LHe provides a cryogenic environment suitable for superconducting coils and particles, enabling magnetic levitation of micro-particle probes in LHe without physical supports to disturb the flow. In addition to its utility in studying classical high Re turbulence, helium also exhibits remarkable quantum hydrodynamic behavior in its superfluid phase. When the temperature drops below approximately 2.17 K, ordinary liquid helium-4 (He I) undergoes a phase transition into a superfluid state (He II). He II is unique because it acts like two entirely interpenetrating fluids: an inviscid superfluid component, representing the condensate with density ρ_s, and a viscous normal-fluid component, representing the thermal excitations with density ρ_n.[57] The two-fluid nature of He II gives rise to many unique properties. For example, rotational motion in the superfluid can only occur via the formation of topological defects known as quantized vortex lines.[58] These vortex lines, each with a core radius of about 1 Å, carry a single quantum of circulation ($\kappa \approx 10^{-3}$ cm^2/s). As a result, turbulence in the superfluid manifests as a disordered tangle of these quantized vortices, referred to as quantum turbulence.[59] The normal fluid, on the other hand, behaves more classically. However, interactions between the two components, particularly through mutual friction caused by the scattering of thermal excitations off the vortex lines,[60] can significantly influence the dynamics of both fluids. This mutual friction can drastically change the turbulence characteristics and the boundary-layer profile of He II in various flow configurations. As such, it holds considerable fundamental and practical importance for studying boundary-layer turbulence in He II under high Re conditions.

In this paper, we present the design and analysis of the PLV system, integrated with our liquid helium flow visualization facility (LHFVF), which can generate turbulent pipe flows with Re exceeding 10^6.[61] The PLV system uses a compact four-coil setup to create a three-dimensional trap with adjustable size and streamwise gradient, enabling easy particle loading while stably levitating superconducting micro-particles near the pipe wall, preventing them from being swept away by high-Re flows. Comprehensive simulations were conducted to calculate the potential energy of the particles in the magnetic trap and to model their motion under both static and high-Re flow conditions. The results show that when the flow is initiated, the particles move downstream due to the fluid's drag force, undergoing damped oscillations before settling into a new equilibrium position. By measuring the particle's mean displacement, we can determine the drag force and consequently calculate the mean flow velocity at the corresponding levitation height. Furthermore, by introducing random velocity fluctuations into the simulations, we established the correlation between particle position fluctuations and velocity fluctuations in the flow, enabling the evaluation of near-wall velocity fluctuations. The levitation height can be adjusted continuously by tuning the coil currents. Our simulations indicate that the PLV system can measure the velocity field across a wide range of wall units $44 \leq y^+ \leq 4400$. By implementing multiple levitated particles, this system may provide new opportunities to study turbulence structures and correlations in the boundary layer that would be otherwise difficult to achieve.

II. METHODS

A. Liquid helium flow facility and particle levitation

As shown schematically in Fig. 1(a), the LHFVF is a cryostat designed for generating and visualizing LHe pipe flows. This facility

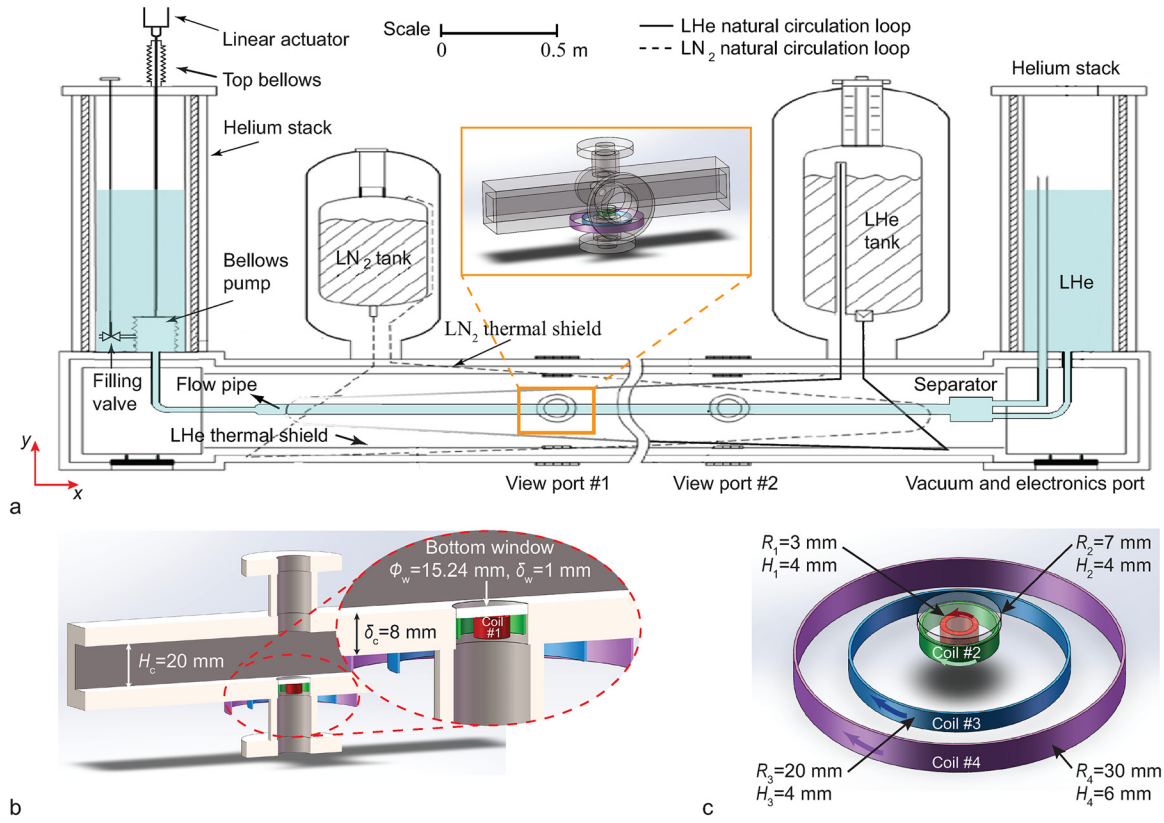

FIG. 1. Pipe flow and particle levitation facility. (a) Schematic diagram of the liquid helium flow visualization facility. **(b)** A schematic showing the locations of the coils for particle levitation. **(c)** A schematic showing the coil specifications.

includes a 5 m-long horizontal cylindrical chamber with an inner diameter of 0.2 m, housed inside the evacuated cryostat body and enclosed by two concentric radiation shields that are cooled by natural circulation loops connected to the liquid helium and nitrogen tanks. A 3.35 m-long pipe with a square cross section (2×2 cm^2) is positioned at the chamber center, connected to helium storage stacks at both ends, where the LHe temperature is controlled by regulating the vapor pressure. The system is equipped with three sets of windows: two vertical sets to allow laser beams to pass through the top and bottom of the pipe, and one side window set for capturing particle motion using a high-speed camera with microscopic lenses. Each set consists of three windows mounted on the vacuum and two radiation shields. To drive the LHe flow, a bellows pump is installed in the left helium storage stack. This bellows pump, with a cross-sectional area of 1.8×10^{-2} m^2 and a stroke length of 9.4 cm, can displace up to 1.7 L of LHe. The bellows is connected to a linear actuator, driven by a computer-controlled stepper motor, capable of producing enough thrust to drive the LHe through the pipe at pipe Reynolds numbers exceeding 10^6.[61]

To probe the flow, we propose to adopt the PLV system, which consists of superconducting niobium particles, i.e., micro-spheres with diameters $d_p = 10$–50 μm, and a superconducting coil system for levitating them. Below its critical temperature $T_c = 9.2$ K, niobium becomes superconducting. At the LHe temperature of 4.2 K, the lower critical field of niobium is about 0.15 T.[62] Below this field strength, the niobium particles exhibit perfect diamagnetism, with a volume magnetic susceptibility χ close to -1 as compared to typical values of -10^{-5} to -10^{-6} for ordinary diamagnetic materials.[63,64] This makes them much easier to levitate using relatively weak magnetic fields. Additionally, niobium is easier to fabricate and machine than many other superconducting materials, making it a practical choice for use in the PLV system.

When a superconducting niobium particle is placed in a magnetic field $\mathbf{B}(\mathbf{r})$, it experiences a potential energy per unit volume given by[65]

$$E(\mathbf{r}) = (\rho_p - \rho_f) g y + \frac{1}{4} \frac{\mathbf{B}^2(\mathbf{r})}{\mu_0}, \tag{1}$$

where $\rho_p = 8570$ kg/m^3 and $\rho_f = 145$ kg/m^3 are the densities of niobium and LHe, respectively, g represents gravitational acceleration, and μ_0 is the vacuum permeability. Levitation of the niobium particle can be achieved at a location where $\partial E(\mathbf{r})/\partial z = 0$. For stable levitation, $E(\mathbf{r})$ must increase in all directions from the levitation location.

Given the LHe environment, we choose to use superconducting coils to generate the magnetic field to avoid Joule heating. There are various design constraints to consider: the coils must fit around the window flange of the flow pipe, and the current in the coil wires must remain below the critical current to maintain the superconducting state. At the same time, the coils must provide a strong magnetic field gradient in both the vertical and the flow directions to levitate the

niobium particles and to prevent the particles from being swept away by LHe in high Re flows. After thoroughly evaluating various coil configurations and current settings, we finally arrived at the optimal coil design, as illustrated schematically in Figs. 1(b) and 1(c).

This coil system consists of four concentric coils, coaxially aligned with the bottom window. Coils #1 and #2 are installed inside the window flange just below the 1-mm-thick bottom window, while coils #3 and #4 are placed outside the window flange beneath the flow pipe. The radii of coils #1, #2, #3, and #4 are 3, 7, 20, and 30 mm, respectively. Each coil is constructed using copper-niobium titanium wires from SUPERCON Inc., capable of carrying up to $I_c = 6.8$ A at 4.2 K,[66] with $T_c = 9.6$ K and $B_c = 8$ T. Coils #1, #2, and #3 each consist of 15 layers with 40 turns per layer, yielding a total of $N_1 = N_2 = N_3 = 600$ turns per coil. With a wire thickness of 102 μm, 40 turns in each layer results in a coil height of 4 mm. Coil #4 also has 15 layers but 60 turns per layer, rendering a total of $N_4 = 900$ turns and a coil height of 6 mm. To ensure the wires remain in the superconducting state, the coil region is thermally anchored to the LHe environment. The current leads are constructed with optimized copper segments and incorporate two interstage thermalizations, one at the 77 K shield and another at the LHe bellow, to reduce heat conduction to the coils. This design minimizes thermal load and ensures all wires remain well below their critical temperature and magnetic field limits throughout operation. As we will present in Sec. III A, when suitable currents are applied to these coils, a three-dimensional potential trap can form where $E(\mathbf{r})$ exhibits a local minimum at the levitation location. As indicated in Fig. 1(c), the current in coil #1 flows in the opposite direction to that in coils #2, #3, and #4. This configuration lowers the potential energy at the trap center while raising it along the sides, creating a pancake-shaped trap elongated in the horizontal direction. This design facilitates easy particle loading and allows for convenient particle displacement control within the trap region, accommodating a wide range of LHe flow speeds.

B. Magnetic field generated by the coils

Consider a single solenoid, which is a cylindrical coil of length $2L$ and radius R, tightly wound with closely packed current loops. The solenoid is centered at the origin of a cylindrical coordinate system (ρ, ϕ, z), with its axis aligned along the z-axis. Let I represent the current in each loop, and N denote the total number of loops. The magnetic field generated by this solenoid in three-dimensional space can be calculated using the Biot–Savart law.[67] In terms of elliptic integrals,[68,69] the magnetic field can be expressed as

$$B_\rho = \frac{\mu_0 NIR}{\pi}[\alpha_+ P_1(k_+) - \alpha_- P_1(k_-)], \tag{2}$$

$$B_z = \frac{\mu_0 NIR}{\pi(\rho + R)}[\beta_+ P_2(k_+) - \beta_- P_2(k_-)]. \tag{3}$$

Due to axial symmetry, the B_ϕ component is absent. Functions P_1 and P_2 are defined as

$$P_1(k) = K(k) - \frac{2}{k^2}[K(k) - E(k)], \tag{4}$$

$$P_2(k) = -\frac{\gamma}{1-\gamma^2}[\Pi(1-\gamma^2, k) - K(k)] - \frac{1}{1-\gamma^2}[\gamma^2 \Pi(1-\gamma^2, k) - K(k)], \tag{5}$$

where

$$\alpha_\pm = \frac{1}{\sqrt{\xi_\pm^2 + (\rho + R)^2}}, \quad \beta_\pm = \xi_\pm \alpha_\pm, \quad \xi_\pm = z \pm L, \quad \gamma = \frac{\rho - R}{\rho + R}, \quad k_\pm^2 = \frac{4\rho R}{\xi_\pm^2 + (\rho + R)^2}, \tag{6}$$

and the functions $K(k)$, $E(k)$, and $\Pi(1-\gamma^2, k)$ are the complete elliptic integrals of the first, second, and third kind,

$$\begin{cases} K(k) = \int_0^{\frac{\pi}{2}} \frac{d\theta}{\sqrt{1 - k^2 \sin^2\theta}}, \\ E(k) = \int_0^{\frac{\pi}{2}} \sqrt{1 - k^2 \sin^2\theta}\, d\theta, \\ \Pi(1-\gamma^2, k) = \int_0^{\frac{\pi}{2}} \frac{d\theta}{[1 - (1-\gamma^2)\sin^2\theta]\sqrt{1 - k^2 \sin^2\theta}}. \end{cases} \tag{7}$$

In our analysis, we calculate the magnetic field produced by each superconducting coil $\mathbf{B}_i(\mathbf{r})$, with $i = 1, 2, 3, 4$. The total magnetic field $\mathbf{B}(\mathbf{r})$ is the sum of the contributions from all individual coils, $\mathbf{B}(\mathbf{r}) = \sum_{i=1}^{4} \mathbf{B}_i(\mathbf{r})$.

C. Key parameter specifications for numerical analysis

In our study, we used MATLAB to perform several key calculations: (1) the magnetic field, $\mathbf{B}(\mathbf{r})$, generated by the coils; (2) contour plots of the volumetric potential energy $E(\mathbf{r})$ for superconducting niobium particles in the magnetic field; and (3) the motion of levitated particles under various LHe flows in the pipe. Given the axial symmetry of the coil system, we employed a computational domain of 16×12 mm^2 in the x-y plane, with the x-axis pointing in the flow direction and the y-axis aligned along the coils' axial direction. This domain was discretized using a square grid with a spatial resolution of 10 μm in both directions. For the particle motion calculations, a time step of 50 μs was used. The chosen grid size and time step were validated by confirming that the results were independent of both parameters, ensuring convergence. The particle was assumed to be pure niobium, with a density of 8570 kg/m^3, a critical temperature of 9.2 K, and a lower critical magnetic field of 0.15 T at 4.2 K. The LHe was modeled with a density of 145 kg/m^3 and a kinematic viscosity of 8.929×10^{-9} m^2/s.[53] The friction factor for LHe in high Reynolds number pipe flows has been reported in the literature.[70,71] For instance, for a LHe pipe flow with $\mathrm{Re} = 1.12 \times 10^6$ considered in our analysis, the friction factor is $f = 0.0124$. The particle's levitation point was determined by locating the minimum energy point within the trapping region.

III. RESULTS

A. Particle loading and levitation

1. Particle loading

The niobium particles need to be placed inside the flow pipe before the cryostat is cooled down. During the cooling process, the pipe will be pumped and flushed with helium gas. When LHe starts filling, the liquid may slosh in the pipe. The magnetic trap can be turned on only after the pipe is fully filled with LHe and the

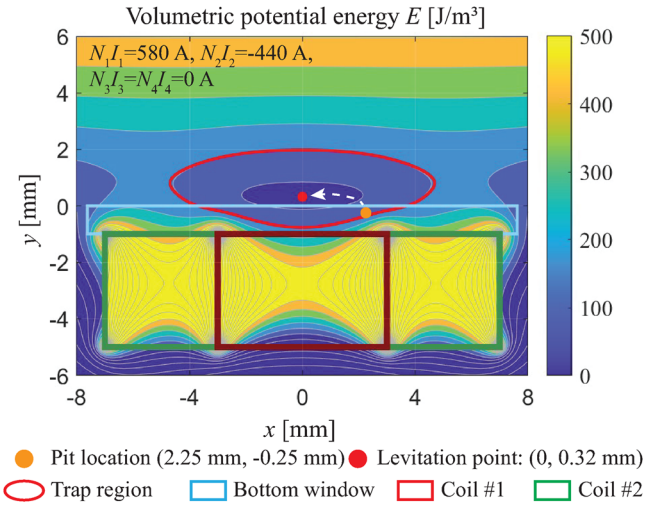

FIG. 2. Contour plot of the volumetric potential energy for particle loading. Configuration where only coils #1 and #2 are activated.

temperature drops below the superconducting transition temperature of the coils. Without the magnetic trap active, the flowing gaseous and liquid helium may carry the particles away from the window region, preventing their levitation in later measurements. To avoid this, a small pit (diameter: 0.5 mm; depth: 0.25 mm) can be carved into the bottom window to securely contain the particles. The pit is located at 2.25 mm downstream from the center of the bottom window. As will be discussed later, the maximum streamwise displacement of the particles in all the considered LHe flows is less than 2 mm from the trap center. Therefore, the pit would not affect the particles during the boundary layer measurements.

After the pipe is filled with LHe and cooled, we can transfer the niobium particles from the downstream pit to the center of the magnetic trap. To accomplish this, we activate only coils #1 and #2 by applying currents of $I_1 = 0.97$ A and $I_2 = -0.73$ A, yielding $N_1I_1 = 580$ A and $N_2I_2 = -440$ A. These currents are well below the critical current I_c of the wire. The method for calculating the magnetic field $\mathbf{B}(\mathbf{r})$ generated by the coils is described in the Method section. Using the computed $\mathbf{B}(\mathbf{r})$, we can produce a contour plot of the volumetric potential energy $E(\mathbf{r})$, as shown in Fig. 2. Given the concentric coil arrangement, $E(\mathbf{r})$ exhibits axial symmetry around the coil center axis. Figure 2 provides a cross section view in the $x - y$ plane, where x is the axis in the flow direction, and the coordinate origin is set at the center of the bottom window surface. As depicted, a region with closed contours of $E(\mathbf{r})$ is formed, where $E(\mathbf{r})$ decreases toward the region center. This is the trapping region, where a niobium particle always experiences a net force directing it toward the center, allowing it to be stably levitated. For clarity, the boundary of the trapping region is marked in red. When only coils #1 and #2 are activated with the specified currents, the radial confinement is relatively weak, and the trapping region extends to a large radius, covering the pit used for niobium particle storage. In this case, a niobium particle initially placed in the pit (the orange dot in Fig. 2) will experience a net lifting force that transports it to the trap center located at ($x_0 = 0$, $y_0 = 0.32$ mm), marked by the red dot.

2. Particle levitation and position control

After the niobium particle is loaded into the center of the magnetic trap, we can activate all four coils to create a more compact trapping region, suitable for flow field measurements in high-Re LHe flows. Figure 3(a) shows a representative contour plot of $E(\mathbf{r})$ with currents $I_1 = 4.00$ A, $I_2 = -2.52$ A, $I_3 = -3.67$ A, $I_4 = -2.89$ A, yielding $N_1I_1 = 2400$ A, $N_2I_2 = -1510$ A, $N_3I_3 = -2200$ A, and $N_4I_4 = -2600$ A. To provide a clearer view of the $E(\mathbf{r})$ profile around the levitation point, Fig. 3 only shows the region near the bottom window and omits the visual representation of coils #3 and #4, although their contribution to $E(\mathbf{r})$ is fully accounted for in the calculations. In this configuration, the particle is levitated at $y_0 = 0.30$ mm. Compared to Fig. 2 where only coils #1 and #2 are activated, the addition of coils #3 and #4 increases $E(\mathbf{r})$ at larger $|x|$ values. This results in a much more compact trapping region with steeper horizontal gradients. As we will discuss in Sec. III B, the viscous drag force on the niobium particle from flowing LHe scales with d_p^2, while the magnetic restoring force, being a body force, scales with d_p^3. When the particle size is small, and the LHe flow speed is high, a significant streamwise displacement of the particle can occur. The strong horizontal gradient of $E(\mathbf{r})$, achieved by activating all four coils, is crucial for confining the particle within the trap region in high-Re LHe flows. The four coil configuration also provides precise control over the height of the levitation point. For instance, Fig. 3(b) shows the contour plot of $E(\mathbf{r})$ with the current in coil #1 remaining the same as in Fig. 3(a) and the currents in coils #2, #3, and #4 decrease to $N_2I_2 = -900$, $N_3I_3 = -1500$, and $N_4I_4 = -2400$ A, respectively. In this case, the height of the levitation

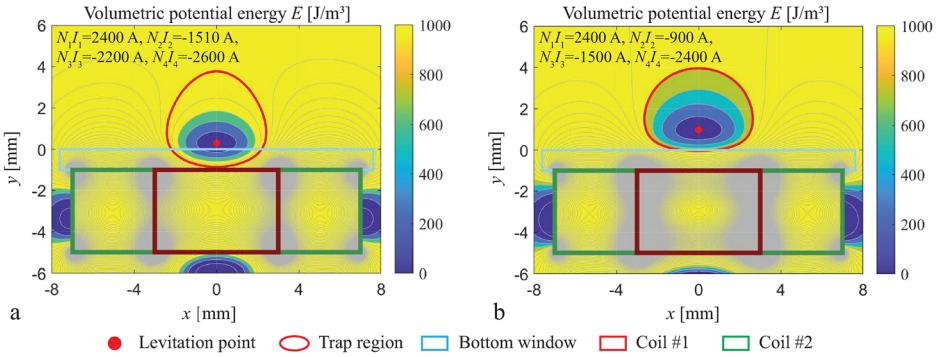

FIG. 3. Contour plots of representative volumetric potential energy fields for particle levitation. (a) Configuration with the particle levitated at $y_0 = 0.30$ mm. **(b)** Configuration with the particle levitated at $y_0 = 0.98$ mm.

point shifts to $y_0 = 0.98$ mm. Our numerical study suggests that the four-coil system enables precise adjustment of the particle levitation height from $y_0 = 20$ μm to $y_0 = 2$ mm for particles with diameters of $d_p = 15$–50 μm, with a tuning resolution two orders of magnitude smaller than the particle size—which ultimately sets the spatial resolution of our flow sensing method. In all the studied cases, the maximum magnetic field strength at the levitation point is 0.014 T, which is far below the lower critical field of niobium. Before using the setup for inferring flow velocities from particle displacements, the simulated energy landscape should be calibrated. By varying coil currents and recording the resulting levitation positions through side-window imaging, we can map current–height relationships and compare them to simulation predictions. Small discrepancies, attributed to geometric uncertainties and coil misalignments, can be corrected by refining simulation parameters, ensuring that the computed energy gradients $\nabla E(\mathbf{r})$ accurately reflect the experimental field. The calibrated $\nabla E(\mathbf{r})$ will later be used to quantify flow-induced forces based on particle motion.

B. Boundary layer study using PLV

1. Study of mean velocity

To illustrate how the PLV system can be utilized for measuring mean velocity profiles in the boundary layer, we begin by considering the equation of motion for the niobium particle, given by

$$\rho_p V_p \frac{d^2\mathbf{r}_p}{dt^2} = [-\nabla E(\mathbf{r})]V_p + \mathbf{F}_d, \tag{8}$$

where $\mathbf{r}_p$ is the position vector of the particle, $V_p = \frac{\pi}{6} d_p^3$ is the particle's volume, $-\nabla E(\mathbf{r})$ represents the volumetric force acting on the particle due to the combined effects of the magnetic field and gravity. The term $\mathbf{F}_d$ represents the drag force exerted by the LHe flow within the pipe. Assuming the flow velocity of LHe at the particle's location is $\mathbf{U}_f$, the drag force $\mathbf{F}_d$ is given by $F_\mathrm{d} = -\frac{3}{4}\frac{C_\mathrm{D}\mathrm{Re}_\mathrm{p}\mu}{d_\mathrm{p}^2}\mathbf{V}$,[72] where $\mathbf{V} = \frac{d\mathbf{r}_p}{dt} - \mathbf{U}_f$ is the relative velocity between the particle and the LHe flow. The drag coefficient C_D can be calculated as[5]

$$C_D \approx \frac{24}{\mathrm{Re}_p} + \frac{6}{1+\sqrt{\mathrm{Re}_p}} + 0.4. \tag{9}$$

In this expression, $\mathrm{Re}_p = \rho_f \mathbf{V} d_p/\mu$ is the particle Reynolds number, where μ is the dynamic viscosity of LHe. Equation (9) applies for Re_p values in the range of $0 \le \mathrm{Re}_p \le 2 \times 10^5$, which is valid for all the flows considered here.

Assuming a niobium particle initially held stationary at the center of the magnetic trap, Eq. (8) allows us to simulate its motion when a LHe flow is turned on at $t = 0$. As an example, Fig. 4 shows the time evolution of the coordinates $x_p(t)$ and $y_p(t)$ for a particle with a diameter of $d_p = 50$ μm, initially levitated at $x_p(0) = x_0 = 0$ and $y_p(0) = y_0 = 0.98$ mm. This simulation is based on a local flow velocity of $U_f = 0.47$ m/s in the x direction. Due to the drag force, the particle drifts downstream and exhibits a damped oscillation around the new equilibrium location at $x_{eq} = 1.04$ mm. The drift in the y direction is negligible, and the oscillations are significantly weaker in this direction. To characterize the damping, we introduce a damping timescale τ_0, defined as the time it takes for the particle's streamwise velocity to fall below 10^{-4} m/s. By this time, all the oscillations around the new equilibrium location are considered negligible. For the case shown in Fig. 4(a), τ_0 is about 0.13 s, which is much shorter than the timescale of about 10 s during which a steady flow can be maintained in the pipe by the bellows pump in a single stroke.[73] The downstream displacement of the particle strongly depends on the flow velocity. Figure 4(b) shows the evolution of the streamwise coordinate $x_p(t)$ for the same particle as in Fig. 4(a) but at three different flow velocity U_f. As U_f increases from 0.27 to 0.47 m/s, the equilibrium displacement increases from about 0.4 to 1.04 mm. The correlation between x_{eq} and U_f obtained over the flow velocity U_f ranges from 0.1 to 0.47 m/s, as shown in Fig. 4(c), for the same particle. This correlation can be well described by a second-order polynomial expression, $x_{eq} = aU_f^2 + bU_f + c$, with the coefficients a, b, and c provided in the figure. Therefore, by measuring the downstream displacement x_{eq}, one can use this correlation to determine the corresponding flow velocity U_f, a key concept of PLV. The coefficients a, b, and c depend on the particle size d_p and the initial levitation height y_0, but they can be easily determined through the same analysis for different configurations.

To apply PLV for boundary layer velocity measurements, we can adjust the levitation height y_0 of the niobium particle. The local mean flow velocity varies at different heights, which results in the particle drifting different distances downstream. To illustrate this effect, consider a boundary layer described by the log law,[18,19]

$$U^+ = \begin{cases} 8.7\, y^{+0.137}, & 50 < y^+ < 600, \\ \dfrac{1}{0.42}\ln(y^+) + 5.6, & 600 \leqslant y^+ \leqslant 0.12 R u_\tau/\nu. \end{cases} \tag{10}$$

For a particle levitated at $y_p = y_0$ from the pipe bottom surface, the corresponding wall unit is $y^+ = y_p u_\tau/\nu$, where the viscous velocity u_τ in He II pipe flows can be evaluated as $u_\tau = (\tau_w/\rho_f)^{1/2} = (\frac{1}{8} f U_{avg}^2)^{1/2}$, with U_{avg} being the mean velocity averaged over the pipe cross section,

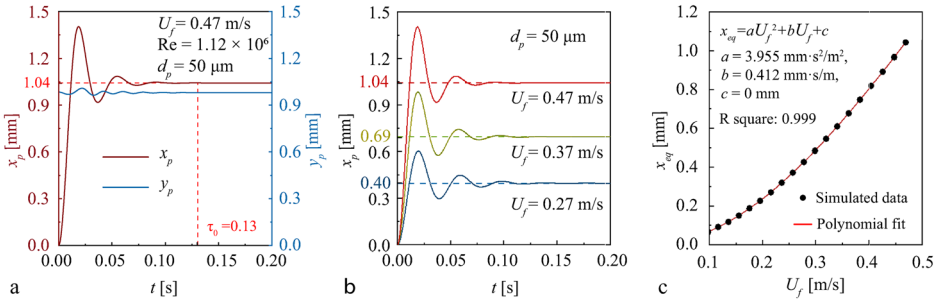

FIG. 4. Position evolution of levitated particles in LHe flows. (**a**) Coordinate evolution for a particle with $d_p = 50$ μm, initially levitated at $y_0 = 0.98$ mm, with a local LHe flow velocity of $U_f = 0.47$ m/s. (**b**) Coordinate evolution of the same particle under different flow velocities. (**c**) Correlation between equilibrium position x_{eq} and local flow velocity U_f.

and f being the measured friction factor for LHe pipe flows.[70,71] Knowing the value of y^+, the dimensionless mean velocity $U^+(y^+)$ can be determined from the above log-law expression. The mean streamwise velocity at height y_p in physical space is then given by $\bar{U}_f(y) = u_\tau U^+(y^+)$. Figure 5(a) shows the evolution of the $x_p(t)$ coordinate for particles with diameters $d_p = 15$–50 μm, levitated at different heights y_p from the bottom window surface in a LHe flow with $U_{avg} = 0.5$ m/s, corresponding to a pipe Reynolds number of $\mathrm{Re} = 1.12 \times 10^6$. The results clearly show that particles of a given size drift different distances depending on their location relative to the wall, resulting in different x_{eq}.

In a real PLV experiment, the process works in reverse. First, a particle is levitated at height y_0, and then the flow is initiated. Once the particle settles at its equilibrium position, the downstream displacement x_{eq} is measured. Using the previously established correlation, the mean streamwise velocity, $\bar{U}_f(y_0)$, can be determined. By varying y_0 and repeating the measurements, a near-wall mean velocity profile can be constructed. Nonetheless, when a particle is placed too close to the wall, the streamwise flow velocity $\bar{U}_f$ becomes too low, resulting in a downstream displacement comparable to the particle's diameter d_p, making it difficult to resolve. Conversely, if the particle is placed too far from the wall, where the flow velocity is much higher, the displacement may exceed the boundaries of the magnetic trap, causing the particle to lose confinement. Since the viscous drag force on the particle F_d scales with d_p^2, while the magnetic restoring force $[-\nabla E(\mathbf{r})]V_p$ scales with the particle volume V_p (and therefore d_p^3), smaller particles tend to drift farther downstream compared to larger particles at a given flow velocity. Therefore, small particles are more suitable for probing the velocity profile near the wall, where the velocity is low. On the other hand, larger particles are better suited for exploring regions farther from the wall, where the velocity is higher and the magnetic trap is less effective at confining smaller particles. In Fig. 5(b), we present the calculated range of the wall unit y^+ that can be explored by niobium particles of four different diameters, i.e., $d_p = 15$, 20, 30, and 50 μm, under the same LHe flow conditions shown in Fig. 5(a). By combining measurements using these different particles, we can explore the mean streamwise velocity $\bar{U}_f(y)$ over a wall unit range of $44 \leq y^+ \leq 4400$, covering the entire logarithmic law region and beyond, as illustrated in Fig. 5(b).

2. Study of turbulence intensity

After the particle settles at its new downstream equilibrium position, x_{eq}, in the presence of a LHe flow, turbulent eddies can cause it to fluctuate around this position. The amplitude of these fluctuations is expected to correlate with the velocity fluctuations, ΔU_f, in the LHe. By measuring the particle's position fluctuations, one can infer ΔU_f, providing insights into the turbulence intensity profile, $\Delta U_f(y)/\bar{U}_f(y)$, within the boundary layer. To demonstrate this, we conducted simulations by introducing random velocity fluctuations, $\Delta U_f(y)$, into the mean streamwise velocity, $\bar{U}_f(y)$, in the equation of motion for the niobium particle (i.e., Eq. (8)). Near the solid wall, turbulence is anisotropic, with streamwise velocity fluctuations dominating the other two directions.[4] In our simulation, we adopted streamwise velocity fluctuations, $\Delta U_f(y)$, based on the near-wall turbulence intensity profile reported by Hultmark, *et al.*[7] For instance, for a niobium particle levitated at $y_0 = 30$ μm from the bottom window surface in the presence of a LHe flow with a pipe averaged velocity of $U_{\mathrm{avg}} = 0.5$ m/s, the streamwise velocity fluctuation ΔU_f is 0.05 m/s. Figure 6(a) shows the time evolution of the x-coordinate for a particle with diameter $d_p = 15$ μm in such a flow. In this simulation, we varied the flow velocity as $U_f(t) = \bar{U}_f + \Delta U_f(t)$ at each time step $\Delta t = 50$ μs, where ΔU_f follows a normal distribution with a root mean square value $\langle \Delta U_f^2(t) \rangle^{1/2} = 0.05$ m/s. As seen in Fig. 6(a), the particle's x-coordinate fluctuates around the equilibrium location $x_{eq} = 0.87$ mm. By analyzing the fluctuations in the time window from 0.1 to 20 s, we obtain the mean fluctuation amplitude to be $\Delta x = \langle (x - x_{eq})^2 \rangle^{1/2} = 15.5$ μm. For practical PLV applications, a correlation between Δx and ΔU_f is needed. To obtain this correlation, we repeated the simulation by varying ΔU_f in the range of 0.02 to 0.065 m/s. The results are shown in Fig. 6(b), which reveal a strong linear correlation between Δx and ΔU_f as $\Delta x = a\Delta U_f$, with the coefficient $a = 303.52$ μs provided in the figure. Again, the coefficient a depends on the particle size d_p and the initial levitation height y_0. For particles with different sizes and levitation heights, the correlation between Δx and ΔU_f can be determined through similar numerical analysis. By experimentally measuring the fluctuations in particle motion at various levitation heights and applying the corresponding correlation tailored to each height, one can gain a comprehensive understanding of the turbulence intensity profile within the boundary layer.

IV. CONCLUSION

We would like to point out that fluid shear within the boundary layer can induce rotation in a levitated spherical particle. This rotation results in a lift force due to the Magnus effect and can also cause a

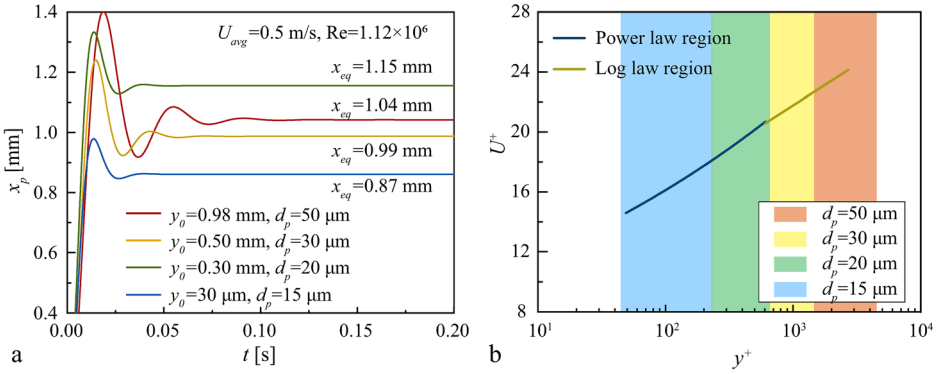

FIG. 5. Boundary-layer mean velocity analysis. (a) Coordinate evolution of particles with different diameters d_p and levitated at varying heights y_0 under the LHe flow with a pipe-averaged velocity of $U_{avg} = 0.5$ m/s. (b) Range of wall units y^+ and the corresponding range of the dimensionless velocity U^+ that can be explored by these particles.

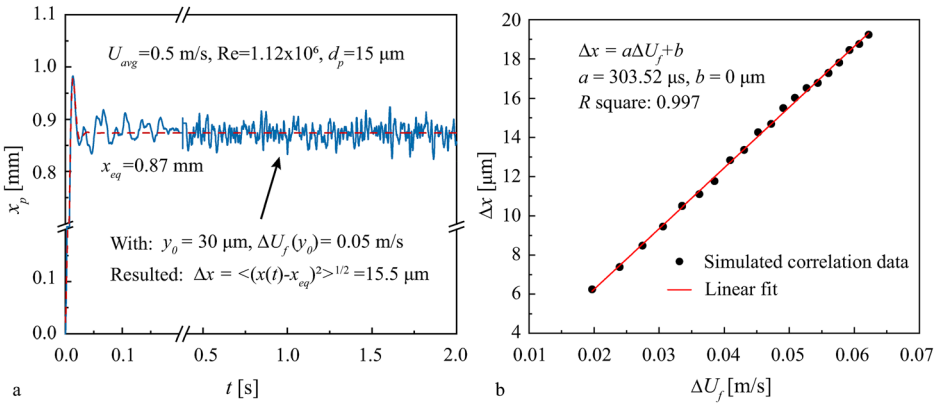

FIG. 6. Boundary-layer velocity fluctuation analysis. (a) Coordinate evolution of a particle with $d_p = 15$ μm levitated at $y_0 = 30$ μm when a random velocity fluctuation with amplitude $\Delta U_f = 0.05$ m/s is added to the local streamwise velocity. The pipe-averaged flow velocity is $U_{avg} = 0.5$ m/s. **(b)** Streamwise position fluctuation amplitude Δx as a function of ΔU_f for the particle considered in **(a)**.

deviation in the drag coefficient C_D from the standard expression given in Eq. (9). These effects become significant for large particles and in regions with high velocity gradients. However, for the micrometer-sized particles considered in our proposed PLV system, we estimate that these deviations are minimal. As introduced by Kurose and Komori,[74] the drag and lift forces on a rotating sphere in a linear shear flow can be characterized using the particle Reynolds number Re_p, a dimensionless flow shear rate $\alpha^* = \frac{a}{U_c}\frac{\partial U}{\partial y}$, and a dimensionless rotational angular speed $\Omega^* = \frac{a}{U_c}\Omega$, where a is the sphere's radius, and U_c is the mean velocity of the fluid along the streamline passing through the sphere's center. For a 10 μm particle levitated 10 μm above the surface, representing a worst-case scenario, we estimate $\alpha^* = 0.15$ and $\Omega^* = 0.075$. At a particle Reynolds number on the order of 1000, which corresponds to the upper end of our operating range, the Magnus effect and particle rotation induce a deviation in the drag coefficient C_D of approximately 2.5% and a lift force equivalent to about 8% of the particle's weight. The quantified estimation supports our claim that rotational and shear-induced forces remain minor under the particle sizes and flow conditions considered in this study. To eliminate the effects of particle rotation due to flow shear, one could consider fabricating the particles to be slightly non-spherical. Non-spherical particles tend to orient in a specific direction within the magnetic trap, effectively preventing undesired rotation caused by the flow. This design strategy may help improve measurement accuracy.

We would also like to highlight that multiple particles with different diameters can be placed in the storage pit from the beginning. Additionally, by coating Teflon or other plastic beads with niobium, it is possible to produce particles with varying overall densities. This introduces an interesting dynamic: particles of the same density but different sizes will be levitated at nearly the same height but displaced to different downstream locations in the presence of LHe flow. Conversely, particles of the same size but different densities would experience similar downstream displacements but would be levitated at different heights. By introducing multiple particles and simultaneously measuring their motion, one can capture both temporal and spatial correlations of velocity fluctuations within the boundary layer. This multi-particle approach offers a unique opportunity to study turbulence structures and correlations in the thin boundary layer, providing a level of detail that is otherwise impractical to achieve. In summary, the combination of the PLV system and the distinctive properties of LHe in a cryogenic environment opens up exciting new possibilities, fully unlocking the potential of LHe in high Reynolds number turbulence research.

ACKNOWLEDGMENTS

Y.Q. and W.G. acknowledge support from the Gordon and Betty Moore Foundation through Grant DOI 10.37807/gbmf11567. This work was conducted at the National High Magnetic Field Laboratory at Florida State University, which is supported by the National Science Foundation Cooperative Agreement No. DMR-2128556 and by the state of Florida. The authors also wish to thank Lauren Roche for her assistance in the design of the superconducting coils.

AUTHOR DECLARATIONS

Conflict of Interest

The authors have no conflicts to disclose.

Author Contributions

Yinghe Qi: Data curation (lead); Formal analysis (lead); Methodology (equal); Writing – original draft (equal); Writing – review & editing (equal). **Wei Guo:** Conceptualization (lead); Funding acquisition (lead); Methodology (equal); Writing – original draft (equal); Writing – review & editing (equal).

DATA AVAILABILITY

The data that support the findings of this study are available from the corresponding author upon reasonable request.

REFERENCES

[1]K. M. Womack, C. Meneveau, and M. P. Schultz, "Comprehensive shear stress analysis of turbulent boundary layer profiles," J. Fluid Mech. **879**, 360–389 (2019).
[2]J. P. Johnston and K. A. Flack, "Review—Advances in three-dimensional turbulent boundary layers with emphasis on the wall-layer regions," J. Fluids Eng. **118**, 219 (1996).
[3]A. J. Smits, B. J. McKeon, and I. Marusic, "High–Reynolds number wall turbulence," Annu. Rev. Fluid Mech. **43**, 353 (2011).
[4]J. Jiménez, "Near-wall turbulence," Phys. Fluids **25**, 101302 (2013).
[5]F. M. White and J. Majdalani, *Viscous Fluid Flow* (McGraw-Hill New York, 2006), Vol. 3.

[6]A. Patel, B. J. Boersma, and R. Pecnik, "The influence of near-wall density and viscosity gradients on turbulence in channel flows," J. Fluid Mech. **809**, 793 (2016).
[7]M. Hultmark, M. Vallikivi, S. C. C. Bailey, and A. J. Smits, "Turbulent Pipe Flow at Extreme Reynolds Numbers," Phys. Rev. Lett. **108**, 094501 (2012).
[8]N. Furuichi, Y. Terao, Y. Wada, and Y. Tsuji, "Friction factor and mean velocity profile for pipe flow at high Reynolds numbers," Phys. Fluids **27**, 095108 (2015).
[9]M. Zagarola, A. Smits, S. Orszag, and V. Yakhot, "Experiments in high Reynolds number turbulent pipe flow," AIAA Paper No. 1996-654, 1996.
[10]J. M. Österlund, A. V. Johansson, H. M. Nagib, and M. H. Hites, "A note on the overlap region in turbulent boundary layers," Phys. Fluids **12**, 1 (2000).
[11]R. Örlü, T. Fiorini, A. Segalini, G. Bellani, A. Talamelli, and P. H. Alfredsson, "Reynolds stress scaling in pipe flow turbulence-first results from CICLoPE," Philos. Trans. R. Soc. A: Math. Phys. Eng. Sci. **375**, 20160187 (2017).
[12]J. P. Monty, "Developments in smooth wall turbulent duct flows," Ph.D. thesis (The University of Melbourne, 2005).
[13]X. Wu and P. Moin, "A direct numerical simulation study on the mean velocity characteristics in turbulent pipe flow," J. Fluid Mech. **608**, 81 (2008).
[14]M. Lee and R. D. Moser, "Direct numerical simulation of turbulent channel flow up to," J. Fluid Mech. **774**, 395 (2015).
[15]Y. Yamamoto and Y. Tsuji, "Numerical evidence of logarithmic regions in channel flow at $R\times et=8000$," Phys. Rev. Fluids **3**, 012602 (2018).
[16]I. Marusic, B. J. McKeon, P. A. Monkewitz, H. M. Nagib, A. J. Smits, and K. R. Sreenivasan, "Wall-bounded turbulent flows at high Reynolds numbers: Recent advances and key issues," Phys. Fluids **22**, 065103 (2010).
[17]B. McKeon and K. Sreenivasan, "Introduction: Scaling and structure in high Reynolds number wall-bounded flows," Philos. Trans. R. Soc. A **365**, 635–646 (2007).
[18]M. V. Zagarola and A. J. Smits, "Mean-flow scaling of turbulent pipe flow," J. Fluid Mech. **373**, 33 (1998).
[19]B. J. Mckeon, J. Li, W. Jiang, J. F. Morrison, and A. J. Smits, "Further observations on the mean velocity distribution in fully developed pipe flow," J. Fluid Mech. **501**, 135 (2004).
[20]H. M. Nagib, K. A. Chauhan, and P. A. Monkewitz, "Approach to an asymptotic state for zero pressure gradient turbulent boundary layers," Philos. Trans. R. Soc. A **365**, 755 (2007).
[21]E.-S. Zanoun, F. Durst, and H. Nagib, "Evaluating the law of the wall in two-dimensional fully developed turbulent channel flows," Phys. Fluids **15**, 3079 (2003).
[22]T. Nickels, I. Marusic, S. Hafez, N. Hutchins, and M. Chong, "Some predictions of the attached eddy model for a high Reynolds number boundary layer," Philos. Trans. R. Soc. A **365**, 807 (2007).
[23]N. Furuichi, Y. Terao, Y. Wada, and Y. Tsuji, "Further experiments for mean velocity profile of pipe flow at high Reynolds number," Phys. Fluids **30**, 055101 (2018).
[24]P. Stainback and K. Nagabushana, "Review of hot-wire anemometry techniques and the range of their applicability for various flows," Electron. J. Fluids Eng. **1**, 4 (1993).
[25]P. Vukoslavčević, J. M. Wallace, and J.-L. Balint, "The velocity and vorticity vector fields of a turbulent boundary layer. Part 1. Simultaneous measurement by hot-wire anemometry," J. Fluid Mech. **228**, 25 (1991).
[26]W. Wilmarth, "Pressure fluctuations beneath turbulent boundary layers," Annu. Rev. Fluid Mech. **7**, 13 (1975).
[27]S. C. Bailey, G. J. Kunkel, M. Hultmark, M. Vallikivi, J. P. Hill, K. A. Meyer, C. Tsay, C. B. Arnold, and A. J. Smits, "Turbulent boundary layer statistics at very high Reynolds number," J. Fluid Mech. **663**, 160 (2010).
[28]Y. Javed, M. Mansoor, and I. A. Shah, "A review of principles of MEMS pressure sensing with its aerospace applications," Sensor Rev. **39**, 652 (2019).
[29]R. J. Adrian *et al.*, "Particle-imaging techniques for experimental fluid mechanics," Annu. Rev. Fluid Mech. **23**, 261 (1991).
[30]B. Van Oudheusden, "PIV-based pressure measurement," Meas. Sci. Technol. **24**, 032001 (2013).
[31]C. M. de Silva, C. M. E. P. Gnanamanickam, C. Atkinson, N. Buchmann, N. Hutchins, J. Soria, and I. Marusic, "High spatial range velocity measurements in a high Reynolds number turbulent boundary layer," Phys. Fluids **26**, 025117 (2014).
[32]F. Scarano, "Tomographic PIV: Principles and practice," Meas. Sci. Technol. **24**, 012001 (2013).
[33]A. Adamczyk and L. Rimai, "2-Dimensional particle tracking velocimetry (PTV): Technique and image processing algorithms," Exp. Fluids **6**, 373 (1988).
[34]D. Dabiri and C. Pecora, *Particle Tracking Velocimetry* (IOP Publishing, 2019).
[35]B. Mastracci and W. Guo, "Exploration of thermal counterflow in He II using particle tracking velocimetry," Phys. Rev. Fluids **3**, 063304 (2018).
[36]B. Mastracci, S. Bao, W. Guo, and W. F. Vinen, "Particle tracking velocimetry applied to thermal counterflow in superfluid ^{4}He: motion of the normal fluid at small heat fluxes," Phys. Rev. Fluids **4**, 083305 (2019).
[37]Y. Tang, S. Bao, T. Kanai, and W. Guo, "Statistical properties of homogeneous and isotropic turbulence in He II measured via particle tracking velocimetry," Phys. Rev. Fluids **5**, 084602 (2020).
[38]Y. Tang, W. Guo, H. Kobayashi, S. Yui, M. Tsubota, and T. Kanai, "Imaging quantized vortex rings in superfluid helium to evaluate quantum dissipation," Nat. Commun. **14**, 2941 (2023).
[39]P. Lavoie, G. Avallone, F. De Gregorio, G. P. Romano, and R. Antonia, "Spatial resolution of PIV for the measurement of turbulence," Exp. Fluids **43**, 39 (2007).
[40]K. Hoyer, M. Holzner, B. Lüthi, M. Guala, A. Liberzon, and W. Kinzelbach, "3D scanning particle tracking velocimetry," Exp. Fluids **39**, 923 (2005).
[41]M. Bross, D. Schanz, M. Novara, F. Eich, A. Schröder, and C. J. Kähler, "Turbulent superstructure statistics in a turbulent boundary layer with pressure gradients," Eur. J. Mech.-B **101**, 209 (2023).
[42]E.-S. Zanoun, C. Egbers, D. Schanz, A. Schröder, E. Öngüner, and M. Dittmar, "Experiments on large-scale structures in fully developed turbulent pipe flow," Eur. J. Mech.-B **102**, 103 (2023).
[43]C. E. Willert, J. Soria, M. Stanislas, J. Klinner, O. Amili, M. Eisfelder, C. Cuvier, G. Bellani, T. Fiorini, and A. Talamelli, "Near-wall statistics of a turbulent pipe flow at shear Reynolds numbers up to 40000," J. Fluid Mech. **826**, R5 (2017).
[44]C. Cierpka, S. Scharnowski, and C. J. Kähler, "Parallax correction for precise near-wall flow investigations using particle imaging," Appl. Opt. **52**, 2923 (2013).
[45]F. Li, H. Zhang, and B. Bai, "A review of molecular tagging measurement technique," Measurement **171**, 108790 (2021).
[46]R. Miles, W. Lempert, and B. Zhang, "Turbulent structure measurements by RELIEF flow tagging," Fluid Dyn. Res. **8**, 9 (1991).
[47]J. B. Michael, M. R. Edwards, A. Dogariu, and R. B. Miles, "Femtosecond laser electronic excitation tagging for quantitative velocity imaging in air," Appl. Opt. **50**, 5158 (2011).
[48]A. G. Hsu, R. Srinivasan, R. D. Bowersox, and S. W. North, "Two-component molecular tagging velocimetry utilizing NO fluorescence lifetime and NO_2 photodissociation techniques in an underexpanded jet flowfield," Appl. Opt. **48**, 4414 (2009).
[49]E. Varga, J. Gao, W. Guo, and L. Skrbek, "Intermittency enhancement in quantum turbulence in superfluid ^{4}He," Phys. Rev. Fluids **3**, 094601 (2018).
[50]J. Gao, A. Marakov, W. Guo, B. T. Pawlowski, S. W. Van Sciver, G. G. Ihas, D. N. McKinsey, and W. F. Vinen, "Producing and imaging a thin line of molecular tracers in helium-4," Rev. Sci. Instrum. **86**, 093904 (2015).
[51]A. Marakov, J. Gao, W. Guo, S. W. Van Sciver, G. G. Ihas, D. N. McKinsey, and W. F. Vinen, "Visualization of the normal-fluid turbulence in counterflowing superfluid ^{4}He," Phys. Rev. B **91**, 094503 (2015).
[52]W. Guo, "Molecular tagging velocimetry in superfluid helium-4: Progress, issues, and future development," J. Low Temp. Phys. **196**, 60 (2019).
[53]R. J. Donnelly and C. F. Barenghi, "The observed properties of liquid helium at the saturated vapor pressure," J. Phys. Chem. Ref. Data **27**, 1217 (1998).
[54]R. J. Donnelly, *High Reynolds Number Flows Using Liquid and Gaseous Helium: Discussion of Liquid and Gaseous Helium as Test Fluids Including Papers from The Seventh Oregon Conference on Low Temperature Physics, University of Oregon, October 23–25, 1989* (Springer Science & Business Media, 2012).
[55]L. Skrbek, J. Niemela, and R. Donnelly, "Turbulent flows at cryogenic temperatures: A new frontier," J. Phys.: Condens. Matter **11**, 7761 (1999).
[56]R. J. Donnelly and K. R. Streenivasan, *Flow at Ultra-High Reynolds and Rayleigh Numbers: A Status Report* (Springer Science & Business Media, 2012).
[57]D. R. Tilley, *Superfluidity and Superconductivity* (Routledge, 2019).
[58]R. J. Donnelly, *Quantized Vortices in Helium II* (Cambridge University Press, 1991), Vol. 2.

[59]W. Vinen and J. Niemela, "Quantum turbulence," J. Low Temp. Phys. **128**, 167 (2002).
[60]W. F. Vinen, "Mutual friction in a heat current in liquid helium II I. Experiments on steady heat currents," Proc. R. Soc. London, Ser. A **240**, 114 (1957).
[61]H. Sanavandi, S. Bao, Y. Zhang, R. Keijzer, W. Guo, and L. N. Cattafesta, "A cryogenic-helium pipe flow facility with unique double-line molecular tagging velocimetry capability," Rev. Sci. Instrum. **91**, 053901 (2020).
[62]A. Ikushima and T. Mizusaki, "Superconductivity in niobium and niobium-tantalum alloys," J. Phys. Chem. Solids **30**, 873 (1969).
[63]M. Yamato and T. Kimura, "Magnetic processing of diamagnetic materials," Polymers **12**, 1491 (2020).
[64]D. Finnemore, T. Stromberg, and C. Swenson, "Superconducting properties of high-purity niobium," Phys. Rev. **149**, 231 (1966).
[65]M. Arrayás, J. L. Trueba, C. Uriarte, and D. E. Zmeev, "Design of a system for controlling a levitating sphere in superfluid 3He at extremely low temperatures," Sci. Rep. **11**, 20069 (2021).
[66]A. Hemmati, S. Fuzier, E. Bosque, and S. Van Sciver, "Drag measurement on an oscillating sphere in helium II," J. Low Temp. Phys. **156**, 71 (2009).
[67]J. Jackson, "A curious and useful theorem in two-dimensional electrostatics," Am. J. Phys. **67**, 107 (1999).
[68]A. Caciagli, R. J. Baars, A. P. Philipse, and B. W. Kuipers, "Exact expression for the magnetic field of a finite cylinder with arbitrary uniform magnetization," J. Magn. Magn. Mater. **456**, 423 (2018).
[69]N. Derby and S. Olbert, "Cylindrical magnets and ideal solenoids," Am. J. Phys. **78**, 229 (2010).
[70]C. J. Swanson, R. J. Donnelly, and G. G. Ihas, "Turbulent pipe flow of He I and He II," Phys. B **284–288**, 77 (2000).
[71]P. Walstrom, J. Weisend II, J. Maddocks, and S. Van Sciver, "Turbulent flow pressure drop in various He II transfer system components," Cryogenics **28**, 101 (1988).
[72]A. Melling, "Tracer particles and seeding for particle image velocimetry," Meas. Sci. Technol. **8**, 1406 (1997).
[73]H. Sanavandi, "Liquid helium turbulent pipe flow and magnetic levitation research," Ph.D. thesis (The Florida State University, 2022).
[74]R. Kurose and S. Komori, "Drag and lift forces on a rotating sphere in a linear shear flow," J. Fluid Mech. **384**, 183 (1999).